Naval Research Laboratory
Washington, DC 20375-5320

All-Metal Flared-Notch Array Radiator for Ultrawideband Applications

RICK W. KINDT
W. RAYMOND PICKLES

Radar Analysis Branch
Radar Division

September 15, 2010

REPORT DOCUMENTATION PAGE

Form Approved
OMB No. 0704-0188

1. REPORT DATE *(DD-MM-YYYY)*	2. REPORT TYPE	3. DATES COVERED *(From - To)*
15-09-2010	Memorandum Report	01-01-2008 to 08-31-2009

4. TITLE AND SUBTITLE

All-Metal Flared-Notch Array Radiator for Ultrawideband Applications

5a. CONTRACT NUMBER

5b. GRANT NUMBER

5c. PROGRAM ELEMENT NUMBER

6. AUTHOR(S)

Rick W. Kindt and W. Raymond Pickles

5d. PROJECT NUMBER
9450

5e. TASK NUMBER

5f. WORK UNIT NUMBER
9450

7. PERFORMING ORGANIZATION NAME(S) AND ADDRESS(ES)

Naval Research Laboratory
4555 Overlook Avenue, SW
Washington, DC 20375-5320

8. PERFORMING ORGANIZATION REPORT NUMBER

NRL/MR/5310--10-9279

9. SPONSORING / MONITORING AGENCY NAME(S) AND ADDRESS(ES)

Office of Naval Research
One Liberty Center
875 North Randolph Street, Suite 1425
Arlington, VA 22203-1995

10. SPONSOR / MONITOR'S ACRONYM(S)

ONR

11. SPONSOR / MONITOR'S REPORT NUMBER(S)

12. DISTRIBUTION / AVAILABILITY STATEMENT

Approved for public release; distribution is unlimited.

13. SUPPLEMENTARY NOTES

14. ABSTRACT

This paper presents simulations and measurements of an all-metal flared-notch array element in both single-polarization and dual-polarization configurations. For broadside radiation, the ultrawideband radiator exhibits an operational bandwidth of 12:1 with active VSWR < 2. The simple-to-manufacture feed consists of a direct coax-to-slot-line transition that mounts directly into the base of the element. The all-metal flared-notch elements are machined from common metal stock and fed via standard SMA coaxial connectors. No soldering is required for any part of the design—including the feed—and assembly is simple and modular. The array parts are machined using a high-precision wire-EDM cutting technology. This precision helps to ensure that measurements (in the 700 MHz to 9 GHz range) are repeatable and give close agreement with theory, even through multiple assembly cycles of the modular construction system. This paper presents results for a 32-element linear array of horizontal elements and also an 8×8 planar array of dual-polarized elements.

15. SUBJECT TERMS

Domain decomposition	Thick flared-notch element	Vivaldi array
Finite element method	Tapered-slot	
Phased array	Ultrawideband arrays	

16. SECURITY CLASSIFICATION OF:			17. LIMITATION OF ABSTRACT	18. NUMBER OF PAGES	19a. NAME OF RESPONSIBLE PERSON
a. REPORT	**b. ABSTRACT**	**c. THIS PAGE**	SAR	30	Rick Kindt
Unclassified	Unclassified	Unclassified			**19b. TELEPHONE NUMBER** *(include area code)* (202) 767-2809

Standard Form 298 (Rev. 8-98)
Prescribed by ANSI Std. Z39.18

Table of Contents

1.   INTRODUCTION

THE flared-notch (Vivaldi) is well known to function very well as an element in ultrawideband (UWB) phased arrays [1, 2]. This radiator has seen wide-spread use for over 30 years and remains popular in part due to its robustness in design and range of manufacturability. Part of its popularity stems from the ease with which inexpensive printed-circuit board (PCB) manufacturing can be used to create large arrays [3, 4]. Over the years, many alternatives to traditional flared-notch designs have been proposed. The balanced antipodal Vivaldi antenna (BAVA) is related to the traditional flared notch but features a somewhat different feed mechanism [5]. As an alternative to PCB designs, all-metal flared-notch radiators provide a different range of manufacturing options and applications [6-9]. Typically the flared-notch class of radiator is considered electrically long – normally a few wavelengths at the highest frequency of operation when a bandwidth of more than 3:1 is desired. However, in recent years, a class of reduced-height radiators has been proposed for which the element length is closer to half a wavelength from the array backplane at the highest frequency of operation. Some of these elements are vertically-integrated such as the reduced-height BAVA [10] and the bunny ear [11, 12]. UWB designs have also been demonstrated using two-dimensional printed surface (or layered substrate) technology, some examples including fragmented apertures [13, 14] and planar dipoles [15, 16]. In general, lower-profile designs exhibit better polarization purity for scans in the D-plane, though VSWR levels tend to be higher than classic flared-notch designs.

   In this paper, a highly-modular, all-metal flared-notch array element is presented that has higher than usual bandwidth. For broadside radiation, the UWB radiator exhibits an operational bandwidth of 12:1 with VSWR < 2 and has VSWR < 1.5 for a large portion of the frequency range. At a 45-degree scan in all planes, the design maintains VSWR < 2 for a full 8:1 bandwidth and 10:1 bandwidth if VSWR < 3 is permissible. Structurally, the element is much thicker than typical flared-notch implementations (approximately 1/3 thickness-to-width ratio). Advantages of thick flared-notch radiators have previously been reported in [17]. This paper reports on both single-polarization and dual-polarization configurations, the details of which were first presented in [18]. The manufactured design operates from roughly 725MHz to 8.9GHz, reducing gradually on the low and high end when scanning. The simple-to-manufacture feed design consists of a direct coax-to-slot-line transition that has been demonstrated to operate over a 12:1 frequency range or better. The all-metal flared-notch elements can be machined from metal sheets and fed via standard SMA coax connectors. No soldering is required for any part of the design, and assembly is simple and modular. In the presented implementation, the parts are machined using a high-precision wire-EDM cutting technology that achieves better than 10-mil tolerances for all dimensions of the machined parts. This precision helps to ensure that measurements (in the 700MHz-9GHz range) are repeatable and give close agreement with theory, even through multiple assembly cycles of the modular construction system.

_____

The main characteristics that make this element unique are the high bandwidth (12:1), the low VSWR (below 2 but well below 1.5 for much of the frequency band), the thicker than usual construction (1/3 thickness-to-width ratio), and the highly-modular, all metal solder-less design. In section II, the details of the mechanical design are presented. In section III, performance characteristics of the design are given, including active VSWR, port isolation, array mismatch efficiency, element gain, and polarization purity. Results are presented for a 32-element linear array and also a dual-polarized 8x8 planar array of elements, comparing measurements with full-wave simulations of the entire finite array structures. Simulation and modeling are performed using the in-house Navy code CEMNAV by author Rick Kindt, which is based on a Domain Decomposition-Finite Element Method (DD-FEM) formulation [19, 20].

2.   MECHANICAL AND ELECTRICAL DESIGN

The array element was designed under the following constraints: (1) it should be all metal, (2) there should be no soldering required for assembly, (3) it should be fed via a standard SMA connector inserted directly/straight into the back of the element, (4) it should operate over the entire 1-8GHz range, (5) it should be dual-polarized, (6) assembly should be modular to make it simple to swap and reconfigure array components, (7) the parts should be machined using high-precision techniques to guarantee repeatable measurements throughout multiple reconfigurations. What follows is the design achieved subject to these constraints.

The element design stems from an application with a need for 8:1 or better bandwidth [21-24]. Fig. 1 shows the profile of the flared-notch radiator, as constructed. The element is approximately 3λ long at the high end of the frequency range and features a slot that meanders to assist with feeding. For this project, two prototype arrays were built – a single polarization 32-element linear array shown in Fig. 2, and a dual-polarized 8x8 planar array of elements shown in Fig. 3. The elements are constructed entirely of metal. For conductivity and weight considerations, 6061 Aluminum was chosen as the base material for construction. The design is modular and constructed to precise tolerances so as to facilitate easy reconfiguration, assembly and disassembly. For the linear array, the circuit path of the antenna is cut from ¼"-thick Aluminum sheet stock as a continuous trace along a single axis. In the case of the 8x8 dual-polarized array, the entire structure is cut from a single block of metal. First, the square cavities created by the intersecting elements are drilled and cut along the z-axis. Next, the circuit paths of the horizontal elements are cut as a continuous trace along the x-axis, followed by the vertical elements cut as a single trace along the y-axis. While the dual-polarized array shown here was cut from a single block of material, it has also been demonstrated that dual-polarized modules can be constructed from machined ¼" Aluminum sheet stock assembled in each polarization [23]. This particular thickness (¼") was chosen because it is possible to drill a 0.162" diameter hole directly into the back of the elements, through which a bulkhead-type SMA connector is inserted and either pressed or bolted in place without the need for soldering. As a result, the elements are structurally much thicker than common embodiments of flared-notch designs, with a thickness of approximately 1/3 of the element width. The added thickness pushes undesirable modes associated with the cavities (formed by the element lattice) well-above the highest frequency of operation. In the final design, the element is roughly $\lambda/2$ wide, $5/32\lambda$ thick, and 3λ long at the high end frequency range.

The design is implemented using SMA connectors to keep the demonstration affordable and interface with readily-available components. SMA connectors cannot be comfortably packed into less than half-inch square grid spacing. With this constraint in mind, the elements have 0.8" lattice spacing, corresponding to half-wavelength-spacing

of 7.4GHz. Though the tolerances are not critical in the linear array, in the dual-polarized design the ports are spaced just close enough that a 5/16 SMA hex nut can turn without interference from the adjacent connector of the other polarization.
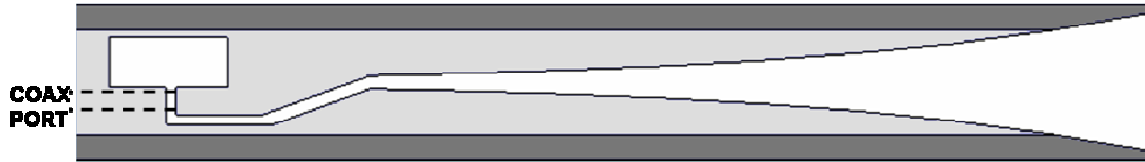

Fig. 1.   Profile of the flared-notch radiator. The length of the element is roughly 3λ at the highest frequency of operation. The taper meanders near the base of the element and meets the slot-line cavity perpendicular to the direction of radiation to assist feed port insertion.

Fig. 2.   32-element linear array of flared notches. The array is constructed from modular sub-arrays of 8 elements.

Fig. 3.   Assembled 8x8 dual-polarized planar array of flared-notches; 128 total ports, 64 in each polarization. The array is modular and can mate in any direction with arrays of the same size to create larger arrays.

A flared-notch antenna works by channeling a signal from a coaxial feed line to the slot-line of the radiating flared notch. Achieving a broadband match between the feed and the radiating slot can be challenging. The simplest and preferred means to feed PCB-based designs is a microstrip-to-slot-line transition using quarter-wave stubs as demonstrated in [25]. More wideband options include the Marchand balun [26] and the double-Y balun, which have been demonstrated to work over bandwidths of 5:1 or better [4]. The main disadvantage is that these techniques require a two-step transition – from coax to microstrip/stripline to radiating slot.

For the element presented here, a simpler feed solution is proposed. The element transfers energy directly from a coax feed to the radiating slot-line with excellent bandwidth and no soldering required. Fig. 4 shows the design of the coaxial section of the feed port. In the implementation, a 0.162" hole is first drilled through the center of the ¼" aluminum stock such that the hole breaches the slot-line wall on the near side, as close as possible to the slot-line cavity at the base of the radiating slot (see Fig. 1). The SMA feed is then inserted into the hole. The center pin contacts the far wall of the slot using a small spring-like device called a "fuzz-button" (currently available from Custom Interconnects). This cylindrical device acts as an extension of the SMA center pin, retaining conductivity and shape under compression. The assembled connector is press-fit and embedded in the port hole using a knurl to hold it in place. Fig. 5 shows the base of the 8x8 array before and after the connectors are embedded. From the figure, it is clear the press-fit components create a very clean design. It was determined through testing that more than 60 inch-lbs of torque could be applied to the connector without the knurl failing – far beyond the torque required to properly seat an SMA cable – at which point the hex nut assembly of the cable would fail (rather than the knurl itself).
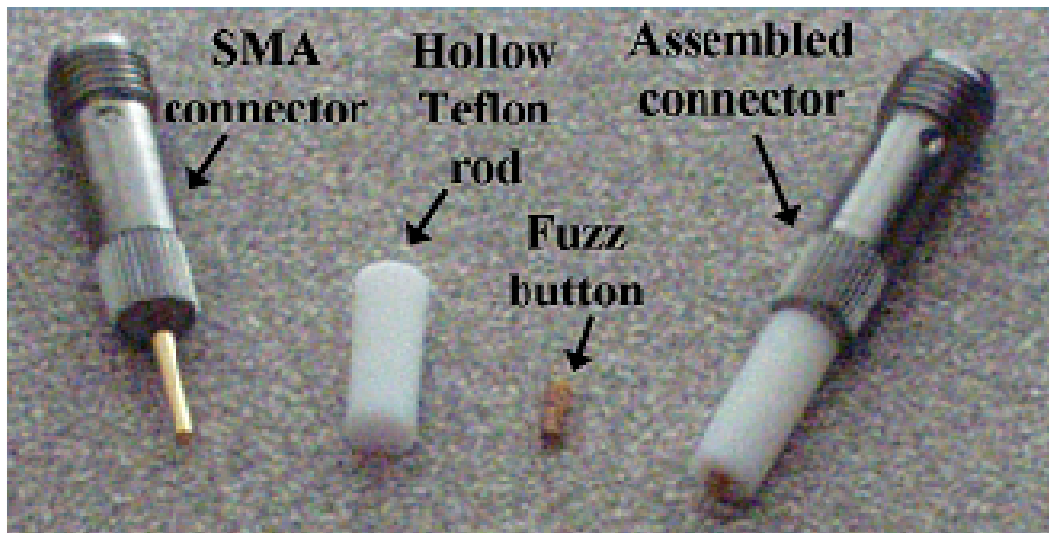

Fig. 4. Design of the element feed for direct coax-to-slot-line transition without soldering. The long outer body of the coax features a knurl that is press-fit into place. The center pin of the coax is extended with a conductive spring-like cylinder (fuzz-button) that achieves contact with the far wall of the antenna slot-line when fully embedded (see Fig. 1 for placement).
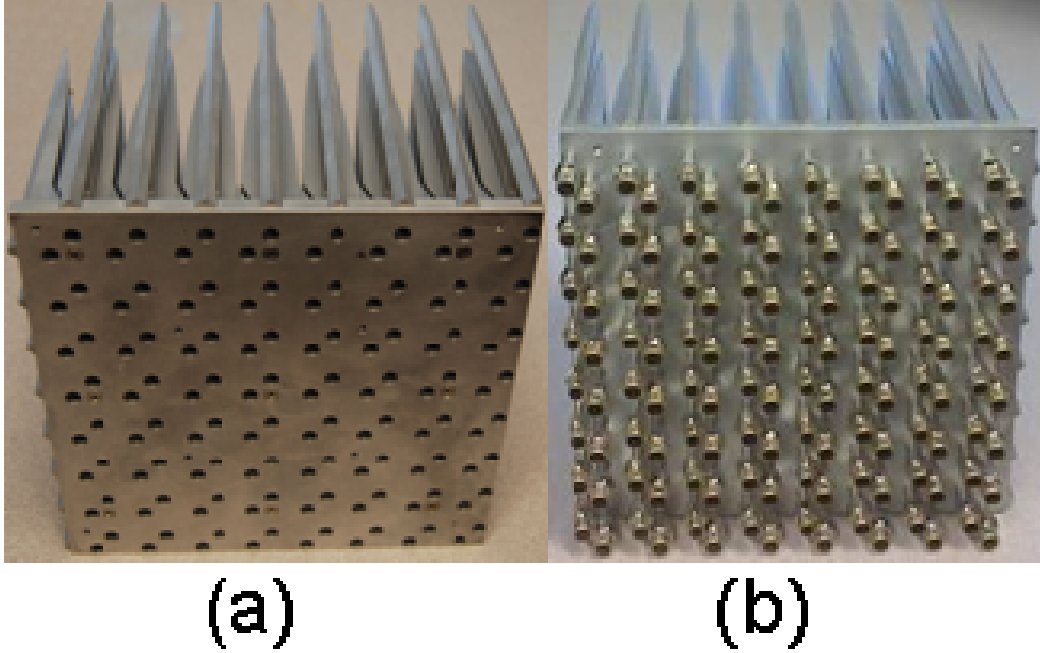
5

Fig. 5. Backside of the 8x8 dual-polarized array (a) before and (b) after the ports are embedded. The straight-press connectors give a clean design.

In order to feed the coax straight into the base of the element, it is necessary to bend the slot such that it turns 90 degrees perpendicular to the direction of radiation. In part, this is difficult to do because of the cramped space within the element cell. To compensate, the slot must be meandered as shown in Fig. 1. It has been observed that the meandering slot helps alleviate some of the loss in port isolation that occurs because of field asymmetry introduced by turning the slot 90-degrees to the direction of radiation.

To ensure EMI isolation of the electronics behind the array, a back plate is used. By design, the cavity of the slot-line open is flush with the back plate of the array. This is done because the geometry created by the intersection of the horizontal and vertical elements create square waveguides that can cause scan anomalies. These anomalies differ from those previously identified in the literature [27]. Though they do not seem to cause scan blindness when the back of the array is left open, when the waveguides are closed by the back plate of the array, at certain frequencies a standing wave is created in the waveguides that is out of phase with the fields of the radiating slots. It has been identified that positioning the slot-line cavity as close to the back plate as possible moves the scan blindness to a higher frequency.

Another feature of this design is that the slot-line connects to the slot-line cavity at approximately the center of the cavity, creating symmetry in the cavity fields. As the slot-line insertion point is moved relative to the cavity center, two resonant peaks can be identified in the VSWR response. By positioning the feed point correctly, the resonances partially cancel each other, creating a single peak in VSWR that is narrower and shorter.

The linear array is constructed from 8-element modular sub-arrays. A 32-element linear array is formed from four sub-arrays of 8 elements and fit into a test fixture as shown in Fig. 2. The 8x8 array of dual-polarized elements shown in Fig. 3 is a modular part of a larger array structure, but has undergone performance testing as a stand-alone array, as reported here. The low-end frequency performance of the 8x8 array will be relatively poor because of the small array size.

It is typically accepted that flared-notch arrays require strong coupling between adjacent elements for proper UWB functionality. It was therefore expected that some form of solder, conductive paste, gasket, or spring would be required for improved coupling at the interface between element sub-arrays. However, when tested, the elements fit together very precisely due to the high-precision manufacturing. The parts were simply bolted in place with no additional measures taken to enforce electrical contact between elements. Measurements over multiple assembly/disassembly cycles of the test structures gave very close agreement with theory without any form of additional connectivity assistance between arrays.

3.   RESULTS

A.   *Simulated Results*

This section presents the predicted theoretical performance of the all-metal element design based on an infinite cell (Floquet) analysis [6, 28]. The analysis was performed using an in-house Navy code (CEMNAV-INF) based on the Finite Element Method (FEM) and has been verified to give very similar results to commercial software (e.g. Ansoft/Ansys HFSS) [29]. The electromagnetic CAD models for the element simulations are very accurate representations of the mechanical models used for manufacturing the array. The reference plane of the coaxial feed port used in the simulations correlates approximately with the reference plane for the network analyzer cables used to collect S-parameter measurements. Fig. 6 shows the expected VSWR of an element in an infinite planar array for broadside radiation and scans to 45 degrees in the E-plane, H-plane, and D-plane. The results shown are for the dual-polarized element pair under horizontal polarization, vertical port passively terminated. As a note, the horizontal and vertical elements are geometrically and electrically identical. At broadside radiation, a 12:1 bandwidth is achieved (725MHz to 8.9GHz) with VSWR levels below 2 across the entire band. The element maintains VSWR well below 2 for scans out to 45 degrees in all scan planes over more than 8:1 bandwidth (850MHz to 8.1GHz). If VSWR levels of 3 are acceptable, this can be achieved from 800MHz to 8.4GHz, for more than 10:1 bandwidth. This operational frequency range is reported with the caveat that scanning may be somewhat restricted at the higher frequencies due to the half-wavelength element spacing of 7.4GHz. Further, the low end frequency performance will not be as good for the small array tested here. While VSWR of 2 is the baseline, for most of the operational band the actual VSWR is much lower, i.e. below 1.5, even under scan.
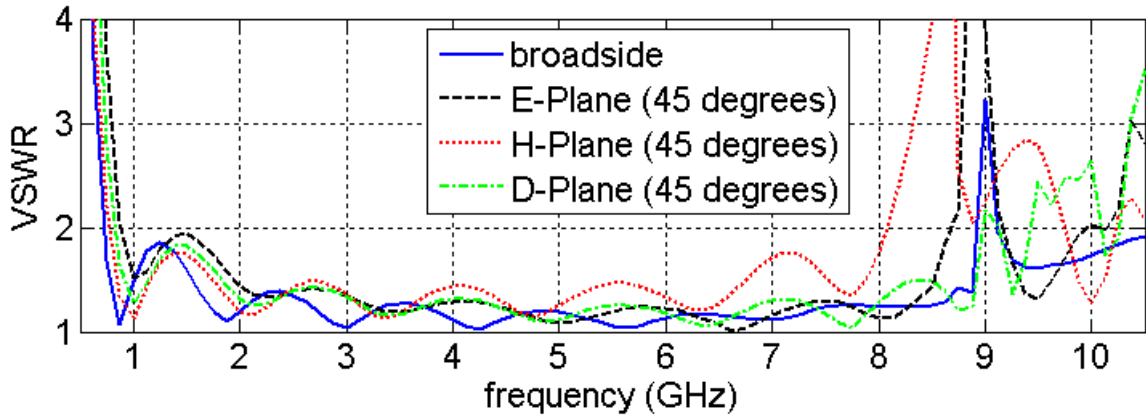

Fig. 6.   Simulated infinite array VSWR performance of the dual-polarized element; results show VSWR < 2 from 725MHz to 8.9GHz at broadside, horizontal polarization. Scan results to 45 degrees show some loss of bandwidth at the high and low end, but with VSWR remaining below 2 for most of the band (1-8GHz). For most of the band, VSWR is below 1.5.
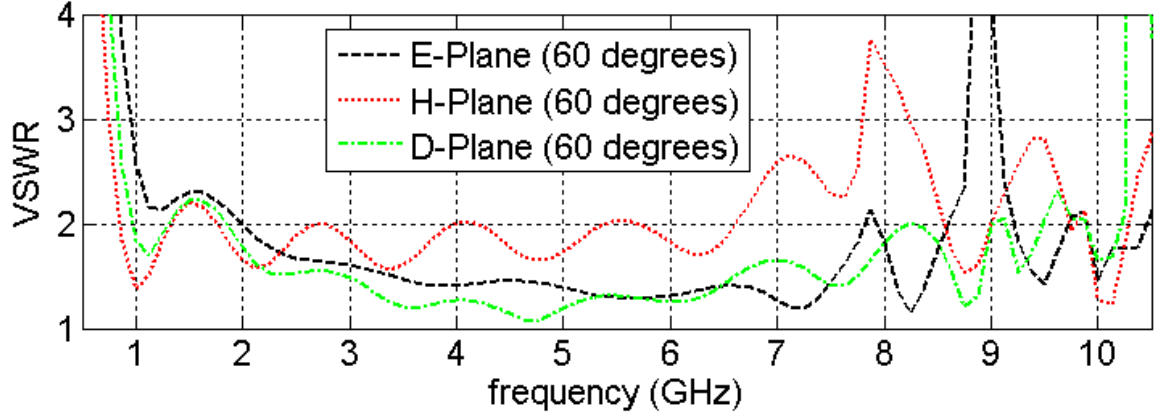
Fig. 7. Simulated infinite array VSWR of the dual-polarized element at a 60-degree scan angle. Results show that VSWR remains well below 3 for most of the operational frequency range.

Fig. 7 shows the simulated VSWR at a 60-degree scan. The VSWR is still below 2 for much of the band, with the exception of the H-plane scan which has slightly-worse degradation. Fig. 8 shows the port isolation for broadside radiation and scan angles at 45 degrees in three planes. This is a measure of energy leaking to the passive vertical port when the horizontal port is active. With the exception of D-plane scanning, isolation is roughly 20dB or better across the band.
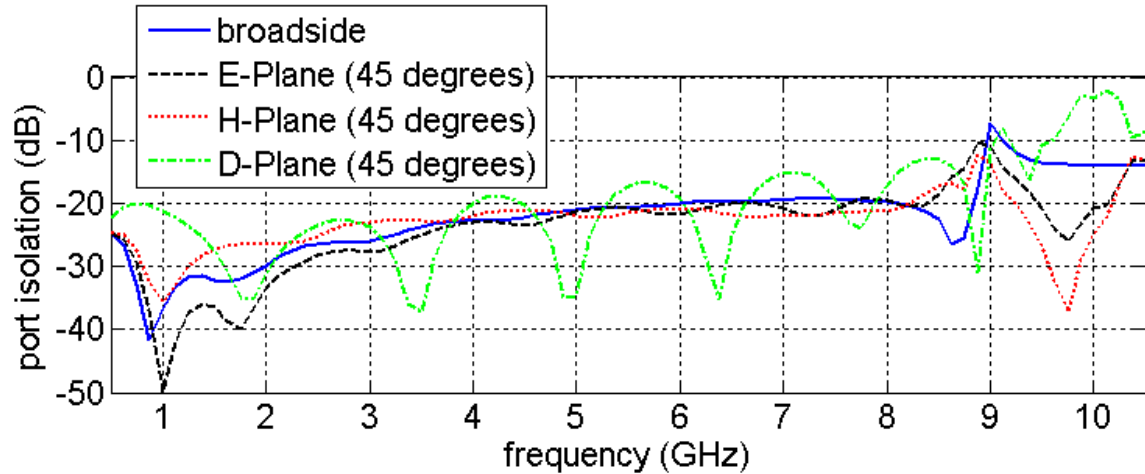

Fig. 8. Simulated S12 (isolation) between vertical/horizontal ports, designed to be roughly better than -20dB across band.

VSWR levels are very similar for both two-dimensional arrays of horizontal elements (i.e. single polarization only) and two-dimensional arrays of dual-polarized elements (i.e. horizontal/vertical element pairs). Linear arrays (as in Fig. 2) function somewhat differently, due to the lack of H-plane coupling. Fig. 9 shows the difference in VSWR levels for these two cases. Where the two-dimensional planar array achieves VSWR < 2 down to 725GHz on the low end, a linear array based on the same element design (and spacing) only achieves VSWR < 2 down to 1.4GHz. This difference was first reported in [24]. However, Fig. 9 shows that the linear array continues to function out beyond well beyond 10.5GHz with VSWR below 2 (for broadside radiation), though in practice,

9

grating lobes would be a problem at these frequencies, limiting scan applications.
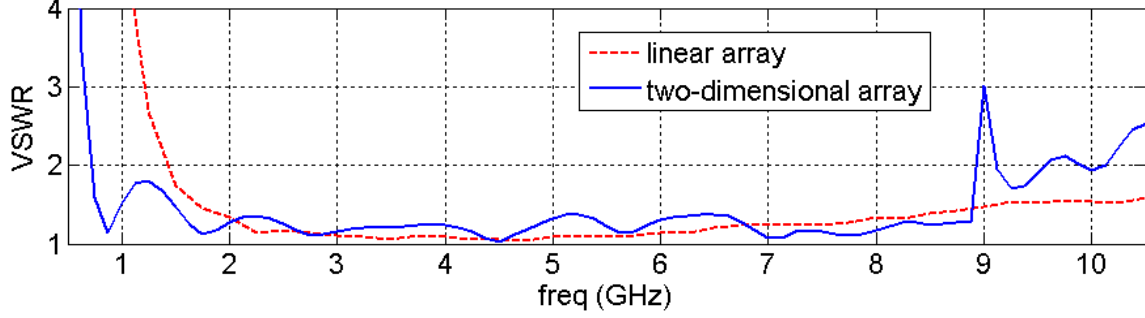

Fig. 9. Comparing the VSWR at broadside radiation for the all-metal element in a linear array versus a two-dimensional planar array; the lack of coupling in the H-plane limits the low-end bandwidth of the linear design.

B. S-Parameter Synthesis, Linear Array

This section presents the measured (active) VSWR for the 32-element linear array and compares the results to full-wave simulations. Measurements of active impedance (and by extension, VSWR) at the element level is performed using an S-parameter synthesis procedure. Consider first a generic N-element array. The active input impedance seen at element x of the array is obtained by synthesizing the active S-parameter (noted as $\bar{S}_{x,x}$) at this element through the superposition of N measurements, i.e., $\bar{S}_{x,x} = \sum\limits_{n=1}^{N} S_{n,x}\psi_{n,x}$, where $S_{n,x}$ is the S-parameter seen at element n with element x excited, all other ports matched. The factor $\psi_{n,x}$ can be used (in post-processing) to adjust the amplitude and phase of individual elements for beam scanning and weighting. Consider now the active VSWR at element 16, near the center of the 32-element linear array. The active VSWR at element 16 is obtained by collecting 32 unique measurements, or specifically: $\bar{S}_{16,16} = \sum\limits_{n=1}^{32} S_{n,16}\psi_{n,16}$), from which the active VSWR is computed. Obtaining a full characterization of the scattering matrix for the 32-element array requires $32(32-1)/2 = 496$ unique S-parameter measurements. Once collected, it is possible to synthesize all combinations of phase scanning and amplitude weighting [30] and predict the VSWR seen at each specific element of the array. It is important to emphasize that this measurement procedure requires that a two-port calibration for non-insertable devices be performed. In other words, assuming all array elements have female connectors, it is not sufficient to do a standard two-port calibration on the usual set of male/female cables and then add a male-male adapter to the female cable post-calibration. This induces a phase error such that S_{11} and S_{22} cannot be added correctly.

The previous section reported on the ideal performance achieved by infinite arrays of the all-metal flared-notch. In this section, measurements on the arrays are presented and compared with full-wave simulations of the complete finite array structures. Here, a

10

different type of analysis tool is used (CEMNAV-DD) based on a non-matching grid Domain Decomposition-Finite Element Method (DD-FEM) [21, 31]. This rigorous design tool allows an engineer to predict with great accuracy exactly how each element in the array will function, giving nearly a one-to-one correspondence between numerical simulations and measurements made in the lab. For standard design procedures (using infinite array simulators) it is typically assumed that finite arrays will perform similar to the infinite design case. Truncation effects associated with finite arrays are not tested and simply treated with known techniques for improving VSWR near array edges. In the past, truncation effects were not tested because codes capable of this type of analysis didn't exist. However, now they do. Here, the use of such a tool is demonstrated in the analysis of complete UWB finite array structures, showing that simulations track very well with measurements, even under high scan angles. For the design engineer, this means that very accurate numerical studies can be performed on finite arrays prior to manufacturing, greatly increasing the chance of critical design flaws being caught early on.

Because they are far from the array edges, elements near the center of the array are expected to perform asymptotically similar to the infinite array case. Fig. 10 shows the comparison of the measured active VSWR at element number 16 (of 32) compared to the infinite array prediction and also the exact finite array simulation (broadside radiation and uniform amplitude weighting). The agreement is very close across the entire measurement band (from 0.5GHz to 10.5GHz), extending above and below the intended operational range of the design (roughly 1-8GHz). Both tools (finite and infinite) do a reasonable job of predicting the VSWR of this element.
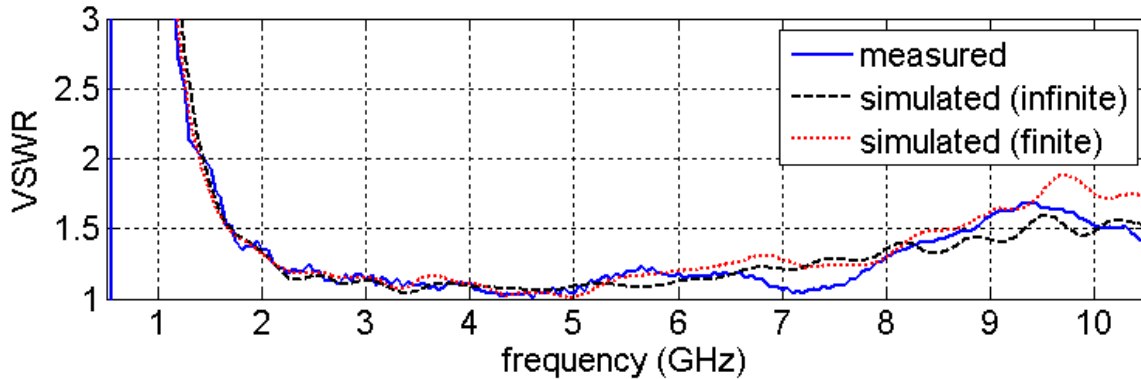

Fig. 10.   Active VSWR of element 16 in the 32-element linear array element at broadside scan and uniform amplitude weighting; exact finite and infinite simulation compared to measurement. Simulations and measurements agree very closely over a wide bandwidth.

Fig. 11 shows the comparison between simulations and measurements at a 45 degree scan. The results are for a positive E-plane scan, though the negative scan is nearly identical. Here, VSWR is below 3 across the frequency band. Again, the results compare very favorably. Additional scan angles were reported here [18].
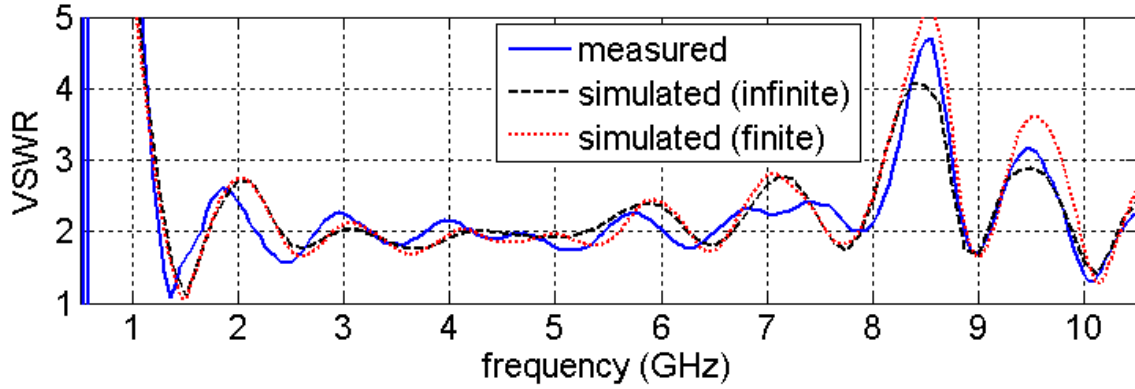
11

Fig. 11. Active VSWR of element 16 in 32-element linear array element, scanned to positive 45 degrees in E-plane; comparison of measured data, infinite array solution, and exact finite simulation. Simulations and measurements track very well under scan.

Fig. 12 shows the measured and simulated VSWR on the first (8) elements of the 32-element linear array. VSWR levels in finite arrays are typically worse near the edge of the array and progressively converge to the infinite array result closer to the array center. What is important to show is that the simulation tools can very accurately predict the VSWR performance of the finite array, including the edge effects. Here, it is shown that simulations give very good agreement for broadside radiation and also the positive 45-degree scan case (scan to the right in Fig. 2). While only one scan case is reported here, several cases were considered and verified to give agreement to measurements. This gives confidence that our simulation tools can be used to validate larger array structures without incurring the cost of building them.
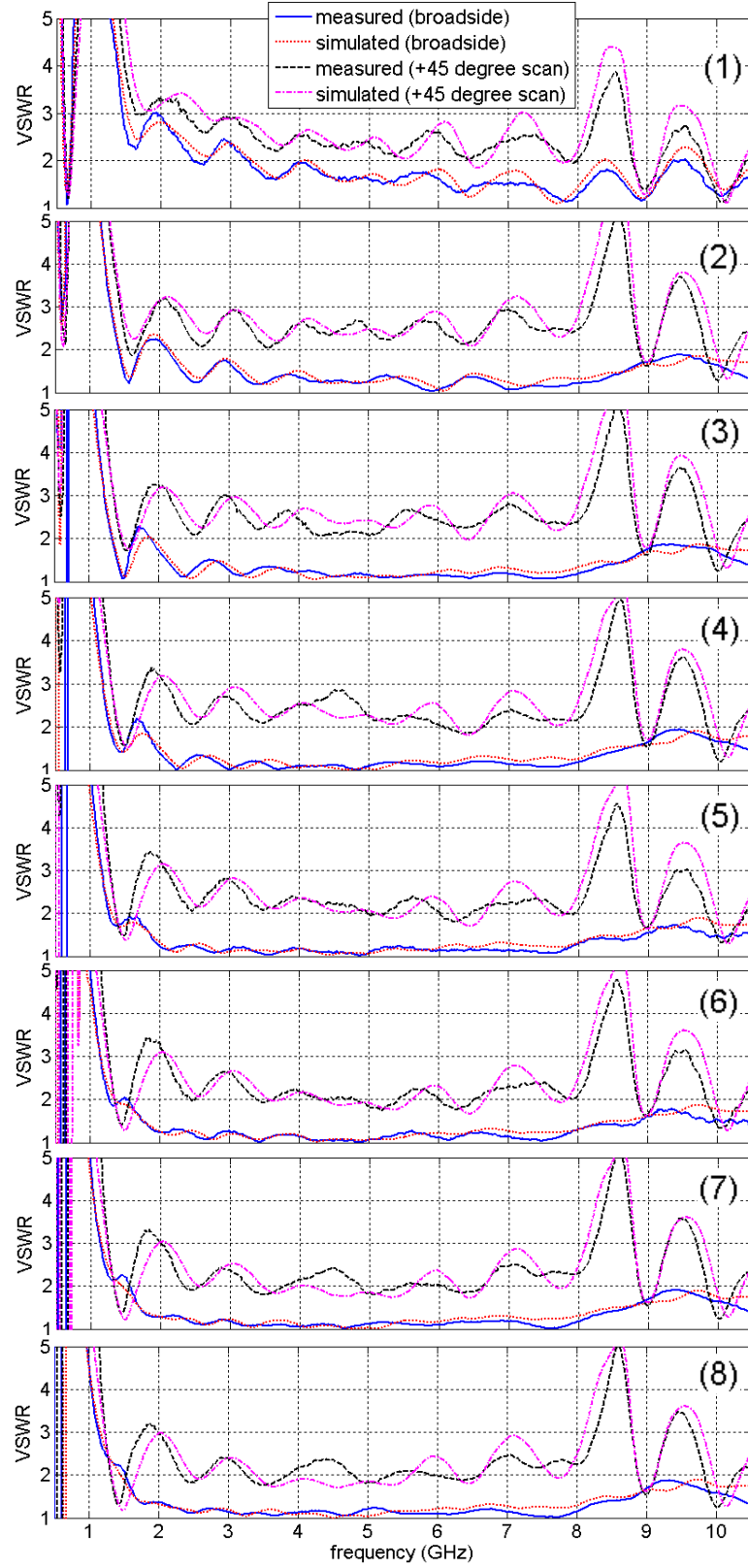
Fig. 12. Measured and simulated active VSWR on the first 8 elements (left-to-right) of the 32-element linear array at broadside radiation and positive 45 degrees. The array functions very much as expected, with

simulated finite array results in very close agreement with measurements. Elements 8-16 of the array have similar VSWR behavior and are not reported.

C.   *S-Parameter Synthesis, 8x8 Dual-Polarized Array*

A similar S-parameter measurement procedure was performed on the dual-polarized 8x8 planar array. For the 8x8 array, in order to synthesize the active VSWR seen at a given element (assuming all other elements of a given polarization radiating), it is necessary to collect 64 S-parameter measurements. Complete characterization of the scattering matrix for this array would require over 2,000 S-parameter measurements for each polarization. To limit the amount of data processing, this paper only reports measurements for the eight elements of row 6 of the array, as depicted in Fig. 13. The results are given in Fig. 14 for broadside radiation and the positive 45-degree E-plane scan case, comparing measurements to a simulation of the 8x8 array using full-wave DD-FEM analysis. As predicted, the VSWR is notably worse than the ideal results given in Fig. 6. While the VSWR is mainly below 2 across the frequency band at broadside radiation – even for this small array – it changes considerably from element to element across the row. At the higher frequencies the VSWR levels are relatively stable and somewhat comparable to the results in Fig. 6. However, at lower frequencies for example, the local maximum in VSWR around 1.3GHz moves around with element position and crests above 2 in some cases (for broadside). Also, there is a dip at the low frequency that reaches down to 675MHz for the elements at the edge (elements 1 & 8). Further, VSWR is not symmetric for positive and negative scans. It is clear from Fig. 14 that the VSWR results are not symmetric across the array for the 45-degree scan case. This is mainly due to truncation effects and also the asymmetry in geometry created by element pairs – for example, the left side of the array is closed off by vertical elements, whereas the right side is not (see Fig. 13). What is perhaps most important is the fact that the full-wave simulation can very accurately predict the measured performance of the array, meaning simulation tools can be used to quantify finite array effects prior to building hardware, minimizing risk. For brevity, only the broadside and positive 45-degree (E-plane) scan case are reported here, though data has been analyzed over a range of scan angles.
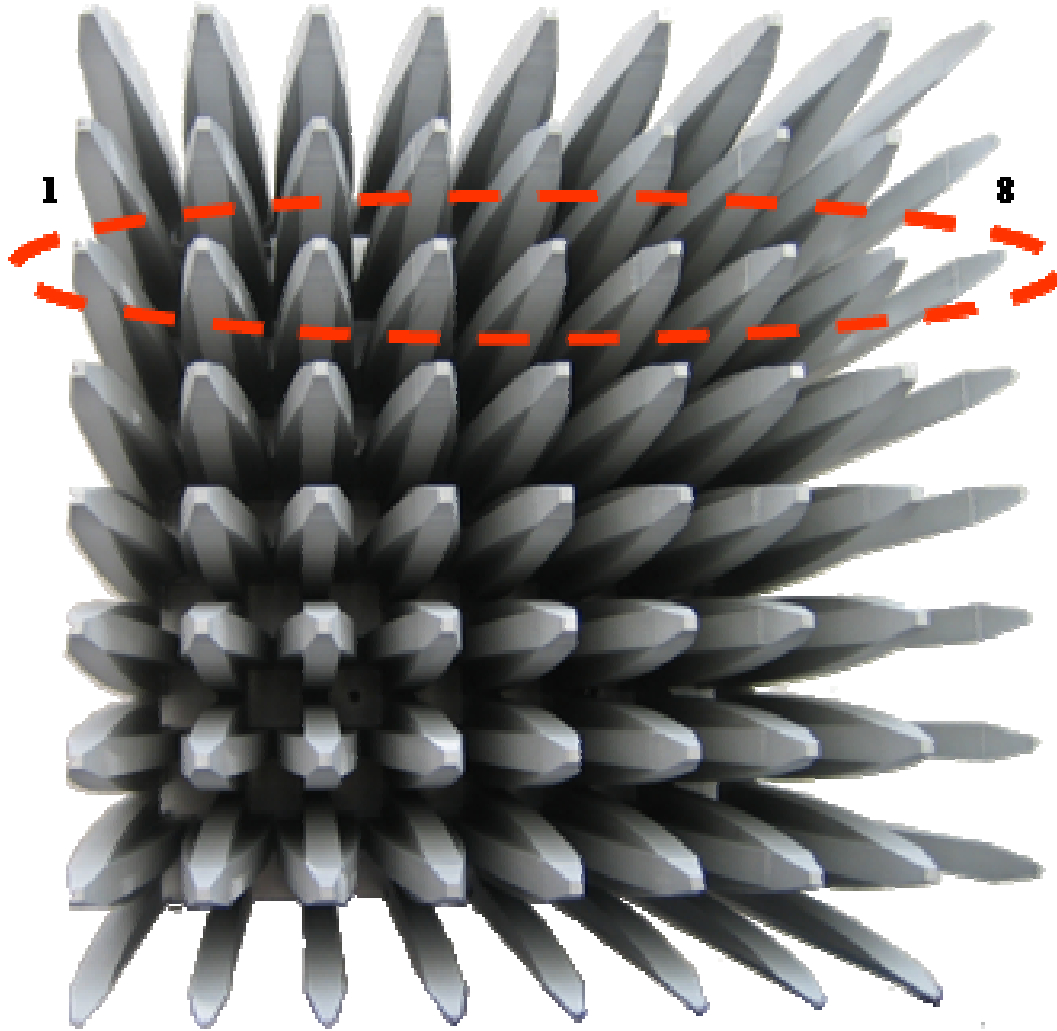
Fig. 13.   Top view of the 8x8 dual-polarized flared-notch array. Circled is row number 6 (with numbering) upon which the S-parameter synthesis measurements were performed.
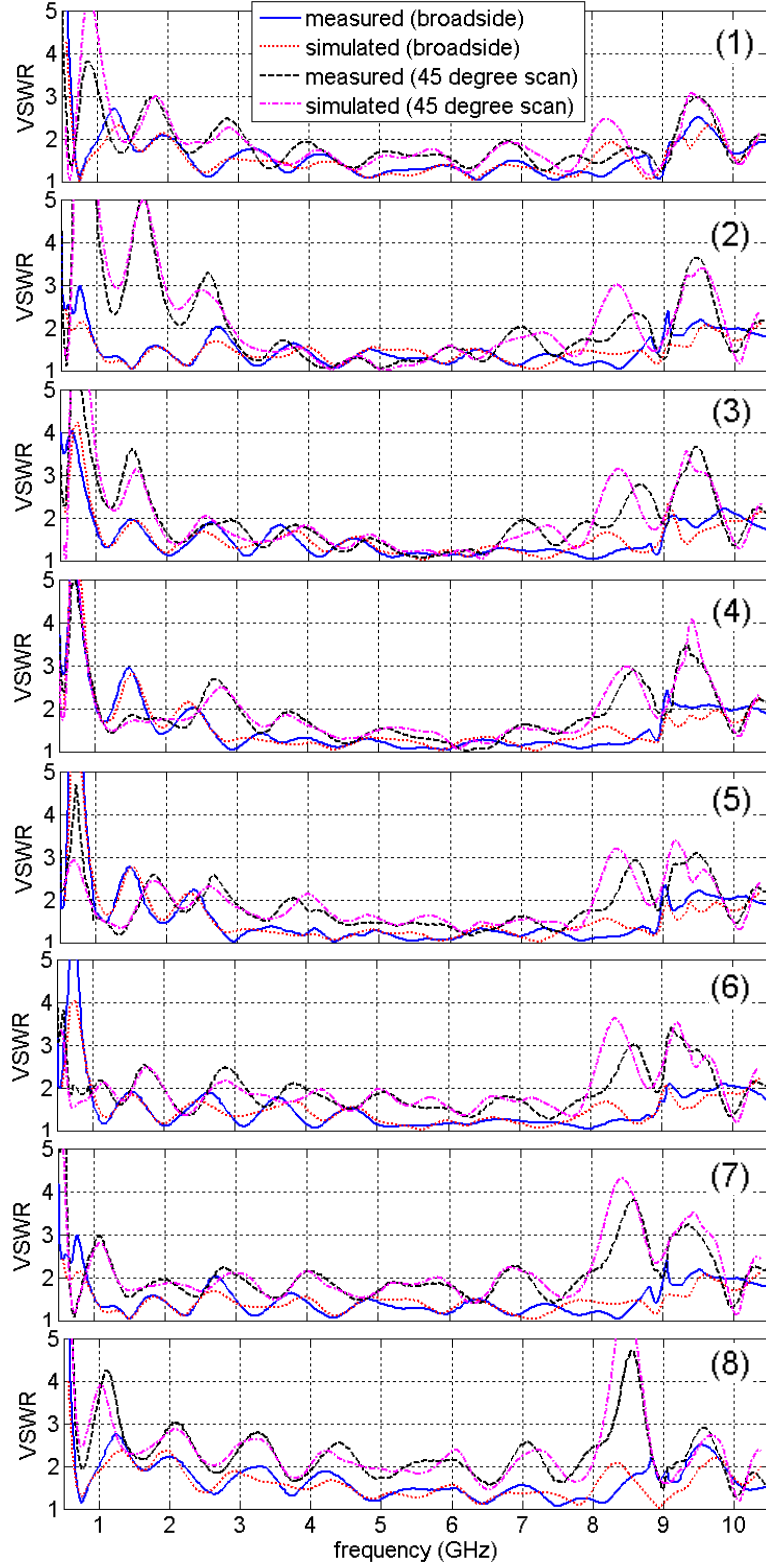
Fig. 14.   Simulated and measured VSWR across horizontal row 6 of the 8x8 array, broadside radiation and positive 45-degrees (E-plane scan). The measurements and simulations are in very close agreement across the entire frequency band.

D.   *Array Mismatch Efficiency*

For finite array analysis it is also important to consider array mismatch efficiency. For antennas, mismatch efficiency is the component of the overall efficiency that relates specifically to impedance mismatch between the antenna port and the feed cable. In finite arrays, this will be dependent on the element position within the array. Therefore, array mismatch efficiency gives the average of this value over the entire array as a single-valued figure-of-merit to gauge how well an array performs at the system level, i.e., as if the entire array were fed via a single port. Fig. 15 shows the computed array mismatch efficiency for the 8x8 array, computed using measured and simulated data. Measurement results are based on data from row 6 only since data for the entire array was not available. Efficiency results for the full array must be simulated (dashed line). The solid (blue) line is the ideal efficiency that can be achieved for very large arrays. In general, the results for the 8x8 array have converged at the higher frequency range (beyond 5GHz), but are typically several percentage points worse than the ideal case at the low end. While this is the general rule, there is a range from 1GHz-1.5GHz where the small finite array has better mismatch efficiency than the infinite case. The important information to glean from the array mismatch efficiency figure-of-merit is that even for the small 8x8 array, the efficiency is better than 90% for almost the entire bandwidth of interest, and is better than 97% for the majority of the frequency band, meaning that on average the system is very well matched.
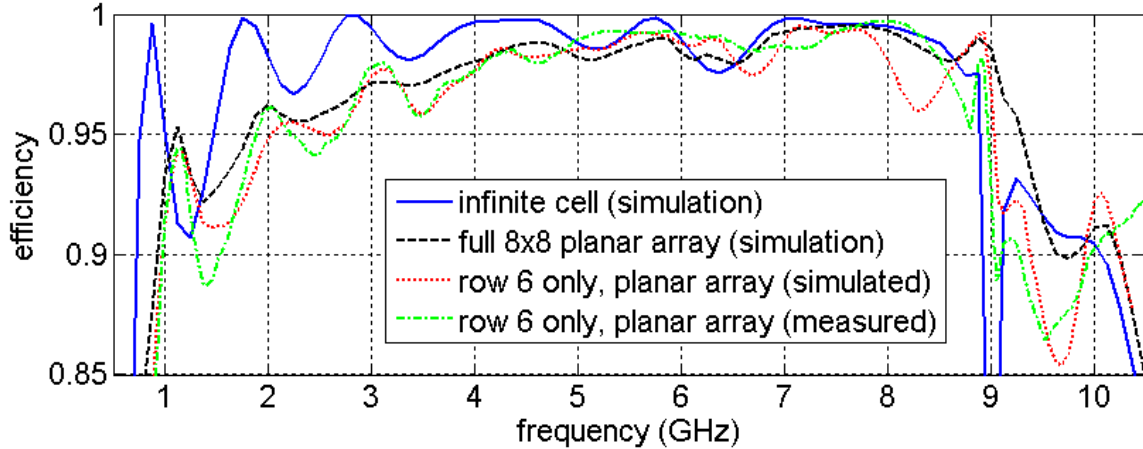

Fig. 15.   Array mismatch efficiency for broadside radiation. The infinite cell (solid line) shows better than 90% efficiency from 725MHz to 8.9GHz with efficiency above 97% for most of the band. The relatively small finite 8x8 array (dashed line) typically shows efficiency number a few percentage points worse than ideal, particularly at the lower frequencies.

To evaluate performance under scan, Fig. 16 gives the mismatch efficiency for various scan angles in the E-plane and H-plane, using measured data from row 6 of the array. For the H-plane, some efficiency is lost when scanning, though even out to 60-degrees, efficiency is generally better than 90% across the band. For the E-plane, scan performance is notably worse. This is in part because row 6 includes E-plane edge elements. Further, there is a notable difference between results for positive vs. negative scan directions, which can mainly be attributed to the asymmetry created by element pairs (i.e., having open ends vs. closed ends of the array).

17

(a) positive E-plane scan

(b) negative E-plane scan

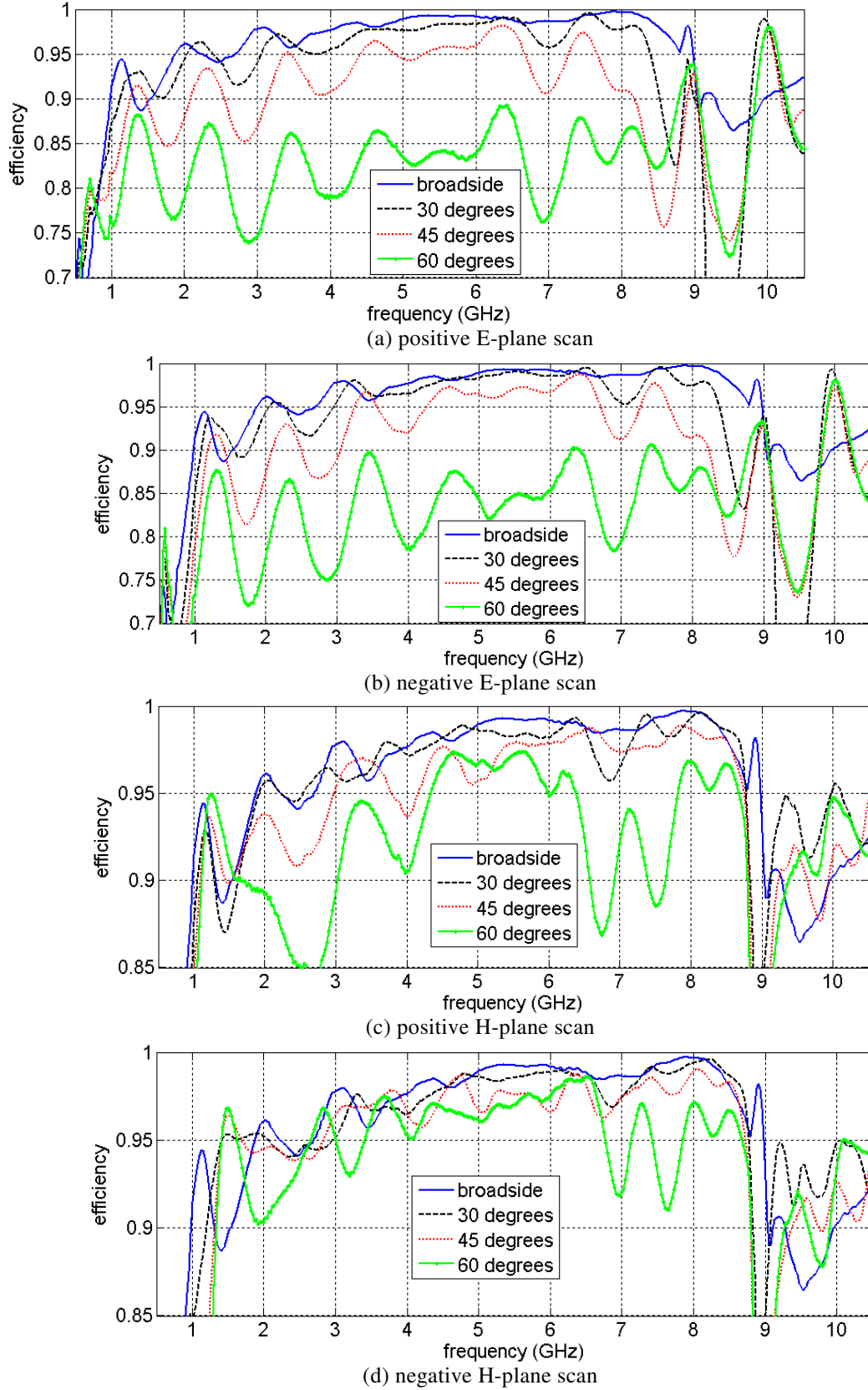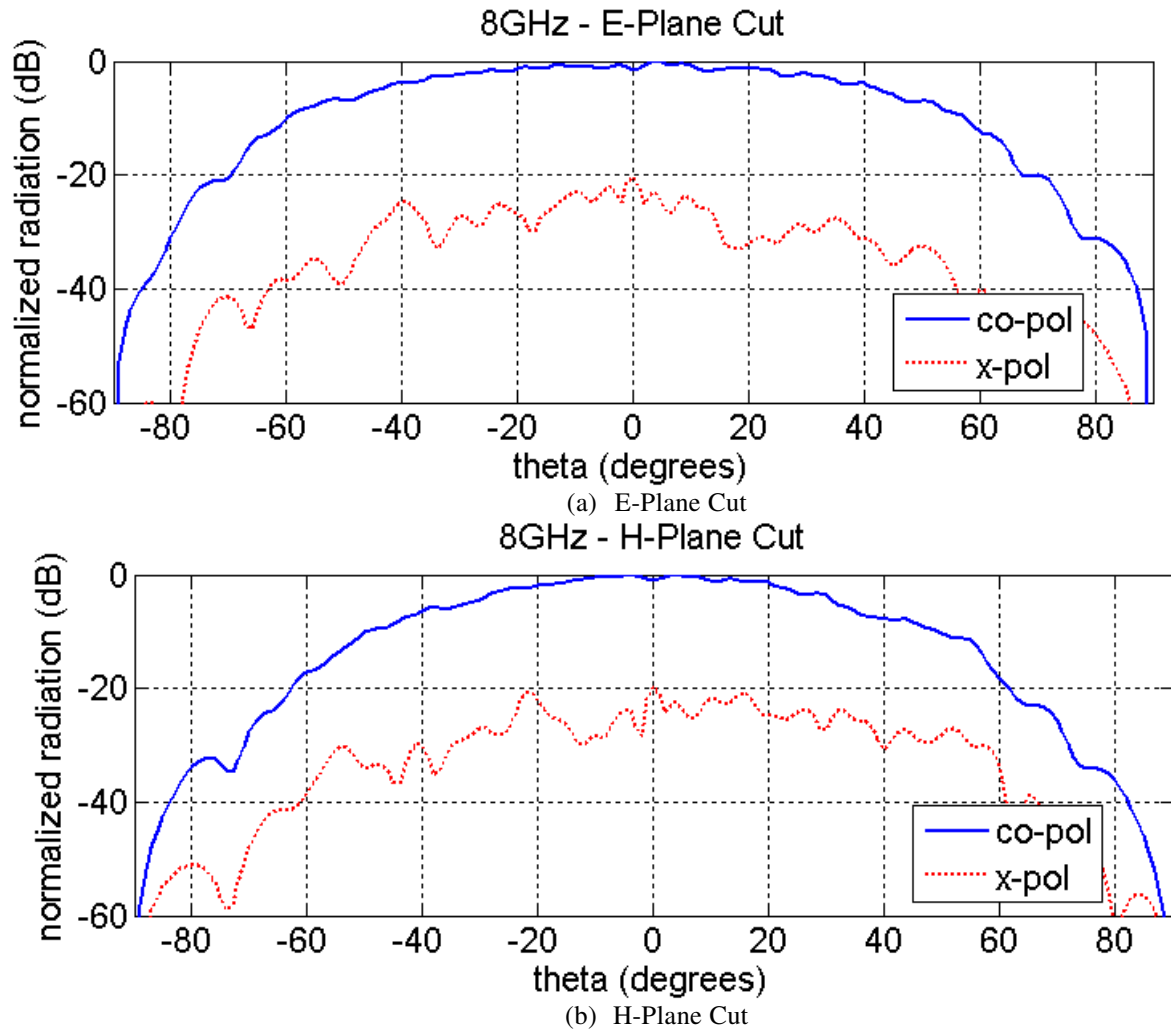(c) positive H-plane scan

(d) negative H-plane scan

Fig. 16. Array mismatch efficiency for various scan angles; results based on measured data from row 6 of the array, so the utility of these results are limited.

18

E.   Element Radiation Patterns

Fig. 17 gives the measured element patterns of the element at 8GHz in the E-Plane, H-Plane, and D-Plane. In the E-Plane and H-Plane the results are typical and consistent for elements of this type – results show better than 20dB of cross-pol. rejection. However, in the D-Plane, the element patterns show that near 45 degrees (theta = +-45, phi = +-45, +-135), there is a null in the co-pol. pattern, such that it dips below the cross-pol. In general, this is typical of radiators that are near three wavelengths long at the half-wavelength spacing. The effect has been observed to lessen as the radiators are made shorter. However, making the radiators shorter can have the effect of reducing the bandwidth, and hence a trade-off must be made. This issue is revisited in a later section on cross-polarization.

(a) E-Plane Cut

(b) H-Plane Cut
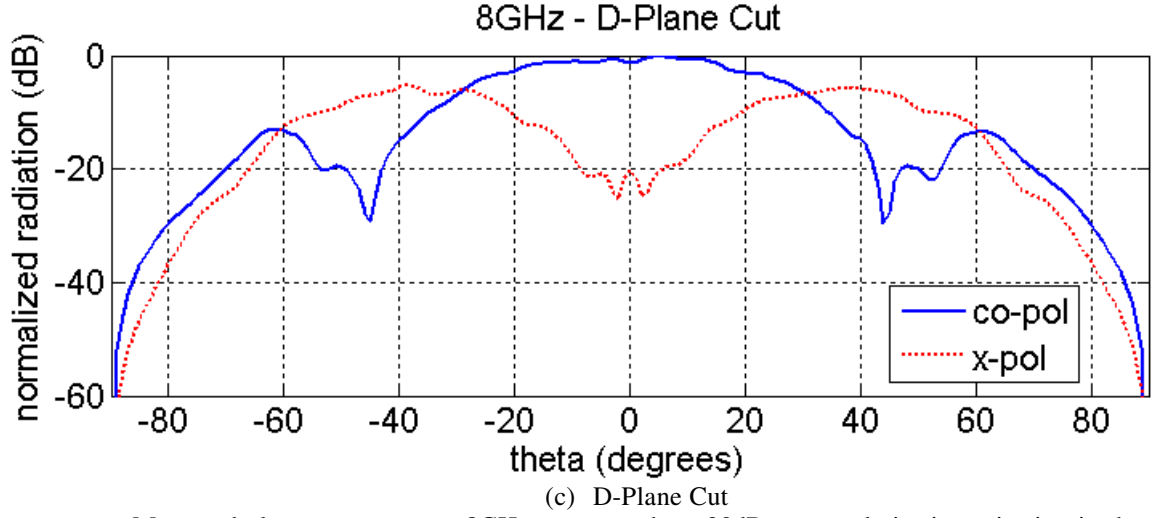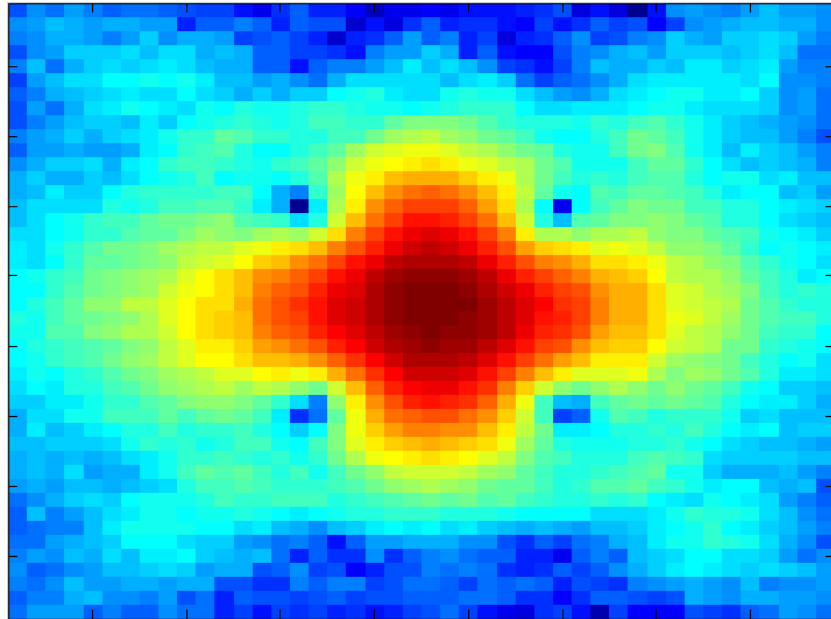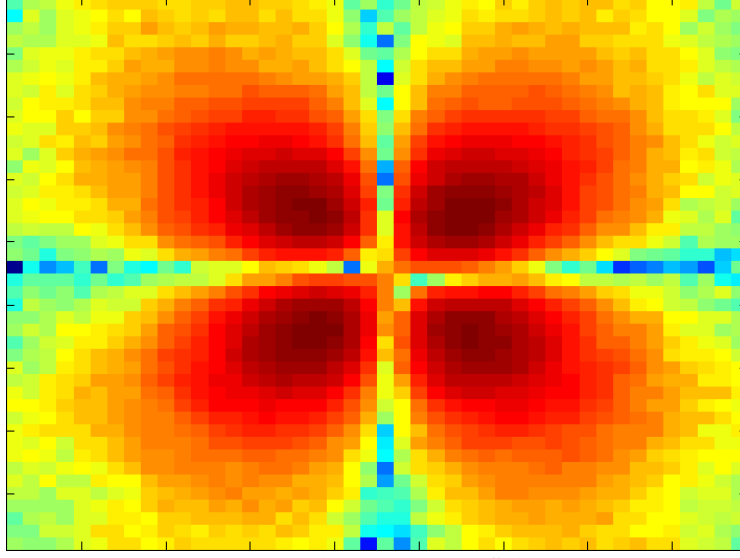
19

8GHz - D-Plane Cut

(c) D-Plane Cut

Fig. 17. Measured element patterns at 8GHz; patterns show 20dB cross-polarization rejection in the principle planes, but in the D-plane, cross-pol. rejection drops to only 10dB at a 20-degree scan, and near 45 degrees, the cross-pol is around 20dB *higher* than the co-pol.

Fig. 18 shows the near-field amplitude data for one of the array elements. The co-pol. pattern clearly shows a wide pattern in the horizontal/vertical planes, but the diagonal cut (corresponding to the D-plane) shows a dimple in the sampled pattern. Further, the cross-pol. data shows a null along the horizontal and vertical axes, with a maximum again in the diagonal plane. The data of Fig. 18 corresponds to the element patterns computed in Fig. 17.

(a) co-pol near-field data

20

(b) x-pol. near-field data

Fig. 18. Measured co-polarization and cross-polarization near-field magnitudes for center element of 8x8 array at 8GHz; x-pol data shows a deep null along the principle axes, but significant lobing in the D-plane; the co-pol data shows wide patterns in the principle cuts, but an anomalous 'dimple' in the D-plane. This near-field data reflects the behavior witnessed in the far-field element patterns.

F. Array Radiation Patterns

Fig. 19 shows the results for the co- and cross-polarization radiation patterns of the 32-element array, measured and simulated at 2GHz. The numerical results are generated using a full-wave simulation of the entire 32-element array including the backplane, using the in-house Navy DD-FEM code. The pattern measurements are collected in a 5'x5' near-field scanner. Several variations of measurement data were collected, including synthesis of composite array patterns from the coherent addition of individual element patterns and also single array patterns formed using static power combiners. In general, the patterns are in good agreement (measured vs. simulated). The lobe structures of the beam match closely, though the simulated cross-polarization levels are somewhat better than the measured results as is typically the case comparing numerical solutions to measured data, since it is much more difficult to achieve perfect alignment/positioning in the lab.
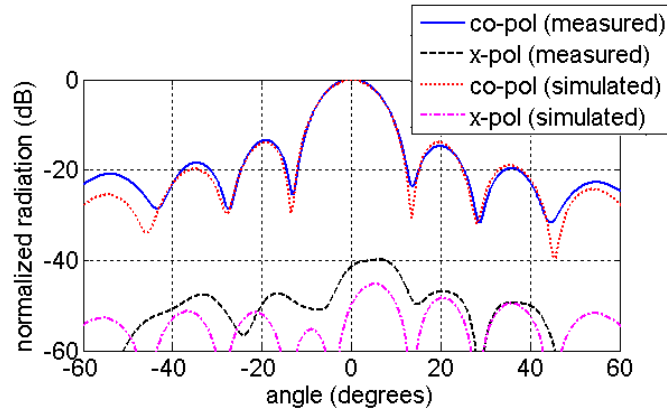
Similarly, the radiation patterns of the 8x8 array are presented at 8GHz. For this case, there were not enough passive beam-forming components on hand to perform a single measurement of the full array in receive mode, as was done for the linear array. Therefore, the measurements of the array were done in receive mode, superimposing stationary element patterns of individual element patterns for each of the 64 array elements. The patterns are fairly typical, and simulations agree reasonably-well with measurements.
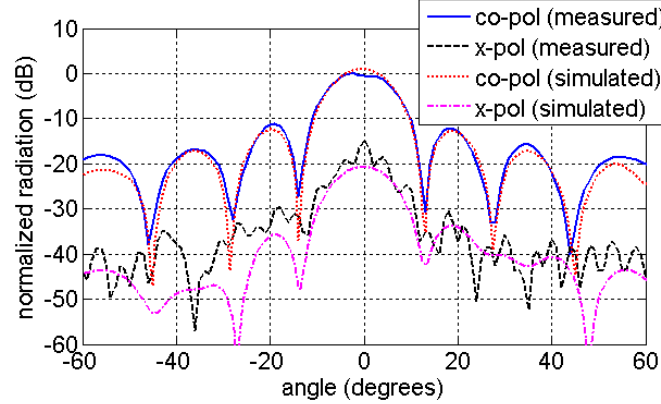

Fig. 20. Measured co-polarization and cross-polarization patterns of the 8x8 array at 8GHz. Patterns are reasonably symmetric and cross-polarization levels are below 20dB.

G. Element Gain

In this section, the element gain vs. frequency is examined. Fig. 21 shows the gain from 0.5GHz to 9.0GHz. The simulated data is computed from the peak gain in the horizontal field levels at broadside, using an infinite cell computation. The measured data is computed from the element in [row,col]=[6,3] of the 8x8 array (see Fig. 13). This element was chosen because it was determined to have the best VSWR behavior in the small 8x8 array. The measured data clearly follows the theoretical trend predicted by the simulation, though some variance in the data was encountered. For the small array, it was found that the element pattern was not smooth and did not consistently give peak gain at broadside, leading to variation in the results. However, the usual gain trend is clear – approximately 5dB of gain at half-wavelength spacing (7.4GHz) falling off gradually towards lower frequencies.
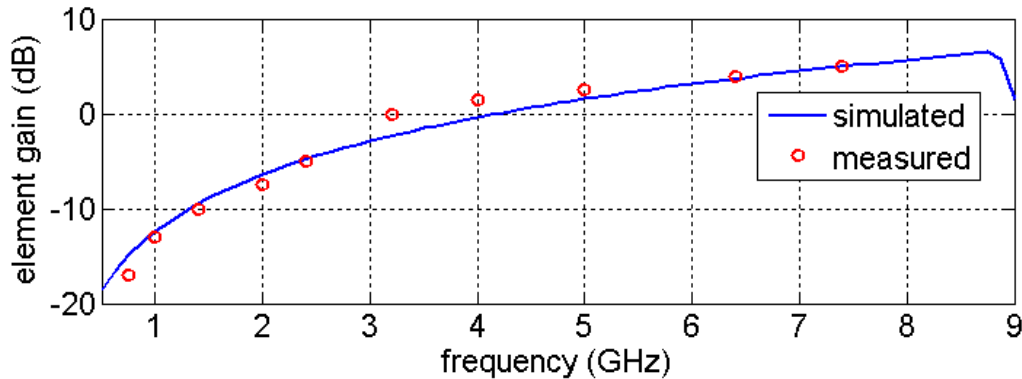

Fig. 21. Simulated and measured gain of the dual-polarized array element.

22

H. Cross-Polarization versus Scan Angle

Cross-polarization is defined as the difference in peak levels of vertically-polarized fields compared to the horizontally-polarized fields in the direction of scan, for horizontal polarization of the active array elements. The beams for the 8x8 array are synthesized from individual element pattern measurements taken in the near-field scanner. Element patterns for both polarizations are taken for each of the individual elements and then superimposed coherently with a phase factor to synthesize a scanning beam. In order for this technique to work correctly, each of the element patterns must be collected under the same set of conditions. This assumes the data sets are collected from the same calibrated collection grid in space and the measurement setup remains stationary (both physically and electrically) during the entire measurement procedure. In theory, while there is a lot of room for user and system error with this procedure, in practice it gives remarkably-repeatable results. Measurements are collected at three frequencies an octave apart – 2GHz, 4GHz, and 8GHz. Cross-polarization data is then synthesized over a range of scan angles in both theta and phi.

TABLE I lists the measured results for the 8x8 array. The simulated results agree with the measurements to within a few dB, and for brevity are not reported. For the given frequencies, cross-polarization levels are the lowest in the E-plane and H-plane – all below roughly 20dB. The worst results show up in the D-plane (phi=45). At 8GHz, the cross-polarization levels are as much as 12dB higher than the co-polarization patterns for higher scan angles. It should be noted that the element spacing in the D-plane is more than half a wavelength at this frequency. It is well known that arrays of flared-notches have good polarization purity in the principal planes with typically worse purity in the D-plane. It has been observed in both measurements and simulations that cross-polarization is better for shorter elements of the same general design, at the expense of bandwidth.

TABLE I
MEASURED CROSS-POL LEVELS VS. SCAN ANGLE FOR THE 8X8 ARRAY

phi (degrees)		0			45			90		
freq. (GHz)		**2**	**4**	**8**	**2**	**4**	**8**	**2**	**4**	**8**
	-45	-32.6	-30.7	-27.9	-6.3	2.0	11.3	-17.8	-18.3	-19.6
	-30	-40.8	-30.4	-37.5	-11.6	-6.1	0.3	-22.1	-20.7	-22.0
theta	**-15**	-34.5	-29.8	-30.7	-24.8	-17.2	-11.6	-27.4	-29.3	-21.2
(degrees)	**0**	-29.6	-26.0	-19.6	-29.6	-26.0	-19.6	-29.6	-26.0	-19.6
	15	-29.8	-30.7	-28.5	-23.1	-17.6	-12.3	-31.8	-27.9	-24.6
	30	-31.9	-28.8	-24.0	-14.3	-7.6	1.3	-27.5	-20.4	-18.0
	45	-37.5	-22.8	-17.0	-9.4	0.1	12.0	-23.0	-19.6	-25.2

Measured cross-polarization levels verses scan angle at 2, 4, and 8GHz for the dual-polarized array. The cross-polarization numbers are good in the principle planes (roughly better than 20dB), but degrade significantly in the D-plane. The small array does not scan well at lower frequencies.

4. CONCLUSION

This paper presents an all-metal UWB antenna element with 12:1 bandwidth at broadside scan, and maintains 8:1 bandwidth for 45-degree scans in all planes. The main limitation of the design is the relatively poor cross-polarization performance in the D-plane, which is similar to other electrically long radiators. However, the element has many desirable qualities, including large bandwidth, very low VSWR, modularity and simplicity of construction. The array shows reasonably good performance considering the small size and lack of edge treatment. Parasitic elements surrounding the array would likely improve performance. The reason this design is presented in a small configuration is because it is part of a larger study on low-cost UWB arrays first presented here [23].

This paper clearly shows that full-wave computational tools can be used to accurately predict the performance of finite arrays with complex element designs. While infinite cell analysis remains the most valuable tool for parametric design of antennas, finite array simulators can be used to improve the overall design of array systems, and will likely become an important tool for array design in the future.

5. APPENDIX

A. *Code Validation*

It is standard practice to verify that the results obtained with in-house codes agree with commercial simulation tools. Fig. 22 shows the agreement between the Navy in-house code CEMNAV-INF with commercial tool HFSS [29] on the initial design of the all-metal radiator, planar array case. The codes agree very well, picking up the same important features of the UWB frequency response. There are subtle differences in the port models and the way performance metrics are computed with the two codes, so differences are expected.
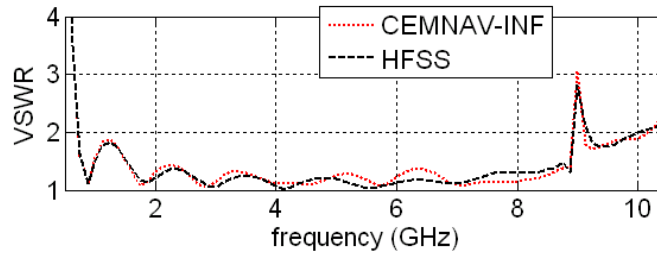

Fig. 22.   Simulated infinite array VSWR performance of the dual-polarized element shows (VSWR < 2 from 725MHz to 8.9GHz). Designs were validated using two codes – an NRL in-house code (CEMNAV-INF) and a commercial package, Ansoft/Ansys HFSS. The codes give good agreement.

6.   REFERENCES

1.   Gibson, P.J., *The Vivaldi Aerial.* Proc. 9th European Microwave Conf., 1979: p. 101-105.
2.   Lewis, L., M. Fassett, and J. Hunt, *A broadband stripline array element.* Dig. IEEE Antennas Propagation Symp., 1974. **12**: p. 335-337.
3.   Holter, H., C. Tan-Huat, and D.H. Schaubert, *Experimental results of 144-element dual-polarized endfire tapered-slot phased arrays.* IEEE Trans. Antennas Propag., 2000. **48**(11): p. 1707-1718.
4.   Kragalott, M., W.R. Pickles, and M.S. Kluskens, *Design of a 5:1 bandwidth stripline notch array from FDTD analysis.* IEEE Trans. Antennas Propag., 2000. **48**(11): p. 1733-1741.
5.   Langley, J.D.S., P.S. Hall, and P. Newham, *Balanced antipodal Vivaldi antenna for wide bandwidth phased arrays.* Microwaves, Antennas and Propagation, IEE Proceedings -, 1996. **143**(2): p. 97-102.
6.   Lucas, E.W. and T.P. Fontana, *A 3-D Hybrid Finite Element/Boundary Element Method for the Unified Radiation and Scattering Analysis of General Infinite Periodic Arrays.* IEEE Trans. Antennas Propag., 1995. **43**(2): p. 145-153.
7.   Trott, K., et al., *Wideband phased array radiator.* Proc. IEEE Int. Symp. on Phased Array Systems and Technology, 2003: p. 383-386.
8.   Holter, H., *Dual-Polarized Broadband Array Antenna With BOR-Elements, Mechanical Design and Measurements.* IEEE Trans. Antennas Propag., 2007. **55**(2): p. 305-312.
9.   Pickles, W.R., et al., *Coincident phase center ultra wideband array of dual polarized flared notch elements*, in *Dig. IEEE Antennas Propagation Symp.* 2007. p. 4421 - 4424.
10.   Elsallal, M.W. and D.H. Schaubert, *Reduced-Height Array of BAVA with Greater Than Octave Bandwidth.* 2005 Antenna Applications Symposium, 2005: p. 226-242.
11.   Lee, J.J. and S. Livingston, *Wide band bunny-ear radiating element*, in *Dig. IEEE Antennas Propagation Symp.* 1993. p. 1604-1607.
12.   Lee, J.J., S. Livingston, and R. Koenig, *A low-profile wideband (5:1) dual-pol array.* IEEE Antennas Wireless Propag. Lett., 2003. **2**(1): p. 46-49.
13.   Friedrich, P., et al., *A new class of broadband planar apertures.* Antenna Application Symp., Allerton Park, IL, 2001: p. 561–587.
14.   Thors, B., H. Steyskal, and H. Holter, *Broad-band fragmented aperture phased array element design using genetic algorithms.* IEEE Trans. Antennas Propag., 2005. **53**(10): p. 3280-3287.
15.   Munk, B., et al., *A low-profile broadband phased array antenna.* Dig. IEEE Antennas Propagation Symp., 2003. **41**: p. 448-451.
16.   Jones, M. and J. Rawnick. *A New Approach to Broadband Array Design using Tightly coupled Elements*. in *IEEE Military Communications conference*. Oct 29-31, 2007 DOI: 10.1109/MILCOM.2007.4454764.
17.   McWhirter, B.T., et al., *THICK FLARED NOTCH RADIATOR ARRAY*, U.S.P. Office, Editor. 1997: USA.

18.   Kindt, R.W. and R. Pickles, *12-to-1 Bandwidth All-Metal Vivaldi Array Element.* Dig. IEEE Antennas Propagation Symp., 2009: p. 1 - 4

19.   Kindt, R.W., *Rigorous Analysis of Composite Finite Array Structures*, in *Ph.D. Dissertation*. 2004, EECS Dept., University of Michigan, Ann Arbor.

20.   Lee, S.C., M. Vouvakis, and J.-F. Lee, *A non-overlapping domain decomposition method with non-matching grids for modeling large finite antenna arrays.* Journal of Computational Physics, 2005. **203**(1): p. 1-21.

21.   Kindt, R.W. and M.N. Vouvakis, *Domain Decomposition Analysis of a Wavelength-Scaled Array (WSA) Architecture.* Submitted to: IEEE Trans. on Antennas and Propagation, August 25, 2009.

22.   Kindt, R. and M. Vouvakis, *Analysis of Wavelength-Scaled Array Architectures via Domain Decomposition Techniques for Finite Arrays*, in *International Conference on Electromagnetics in Advanced Applications*. 2009: Torino, Italy.

23.   Kindt, R. and M. Kragalott, *A Wavelength-Scaled Ultra-Wide Bandwidth Array.* Dig. IEEE Antennas Propagation Symp., 2009: p. 1-4.

24.   Kindt, R., et al., *Preliminary Investigations of a Low-Cost Ultra-Wideband Array Concept.* IEEE Trans. Antennas Propag., 2009. **57**(12): p. 3791-3799.

25.   Shin, J. and D.H. Schaubert, *A parameter study of stripline-fed Vivaldi notch-antenna arrays.* IEEE Trans. Antennas Propag., 1999. **47**(5): p. 879-886.

26.   Marchand, N., *Transmission-Line Conversion Transformers.* Electronics, 1944. **17**: p. 142-146.

27.   Wunsch, G.J. and D.H. Schaubert, *Full and Partial Crosswalls Between Unit Cells of Endfire Slotline Arrays.* IEEE Trans. Antennas Propag., 2000. **48**(6): p. 981-986.

28.   Eibert, T.F., et al., *Hybrid FE/BI Modeling of 3D Doubly Periodic Structures Using Triangular Prismatic Elements and a MFIE Accelerated by the Ewald Transformation.* IEEE Trans. Antennas Propag., 1999. **47**(5): p. 843-850.

29.   *Ansoft High Frequency Structure Simulation (HFSS), Version 11.1*. 2008, Ansoft Corporation.

30.   Hansen, R.C., *Phased Array Antennas*. Wiley Series in Microwave and Optical Engineering, ed. K. Chang. 1998: Wiley-Interscience.

31.   Vouvakis, M.N., *A Non-Conformal Domain Decomposition Method for Solving Large Electromagnetic Wave Problems*, in *Ph.D. Dissertation*. 2005, Ohio State University, Columbus, OH.